

Article

Rational Design of Yolk Core-Shell Structure MnO-Co@C Nanospheres for High-Performance Microwave Absorption

Zhen Xin ^{1,2,3}, Junjie Wu ⁴, Shuchen Sun ^{5,*}, Mu Zhang ^{1,2,3,*} and Xudong Sun ^{1,2,3,*}

¹ Key Laboratory for Anisotropy and Texture of Materials (Ministry of Education), Northeastern University, Shenyang 110819, China

² School of Materials Science and Engineering, Northeastern University, Shenyang 110819, China

³ Foshan Graduate School of Innovation, Northeastern University, Foshan 528311, China

⁴ Sinosteel Engineering & Technology (Inner Mongolia) Co., Ltd., Baotou 014000, China

⁵ School of Metallurgy, Northeastern University, Shenyang 110819, China

* Correspondence: sunsc@smm.neu.edu.cn (S.S.); zhangm@mail.neu.edu.cn (M.Z.); xdsun@mail.neu.edu.cn (X.S.)

Abstract: MnO-Co@C nanospheres were fabricated by in situ polymerizing and high-temperature carbonizing processes. This unique synthesis method does not require any template or reducing gas. The synthesized multicore-shell structure has a shell of about 500 nm and multiple nuclei of several tens of nanometers. Subsequently, extensive experiments were conducted to adjust the material composition of the nanospheres by adjusting the amount of resorcinol and formaldehyde. The results showed that the obtained material performed best when resorcinol and formaldehyde were added to 0.2 g MnCo₂O₄ at 0.3 g and 0.42 mL, respectively. The efficient absorption bandwidth (EAB) value reaches 3.3 GHz when the absorber thickness is 3 mm. The reflection loss (RL) is up to −23.8 dB when the frequency is at 8.6 GHz. The unique yolk core-shell structure gives the material a heterogeneous interface, and the enhanced interfacial polarization loss causes the enhanced dielectric loss. The carbon layer with microporosity also causes conduction loss and multiple reflections. The composite structure formed by metallic Co, MnO, and carbon has better impedance matching and improved microwave absorption capability.

Keywords: MnO-Co@C nanospheres; yolk core-shell; microwave absorption



Citation: Xin, Z.; Wu, J.; Sun, S.; Zhang, M.; Sun, X. Rational Design of Yolk Core-Shell Structure MnO-Co@C Nanospheres for High-Performance Microwave Absorption. *Coatings* **2022**, *12*, 1405. <https://doi.org/10.3390/coatings12101405>

Academic Editor: Rafael L. Quirino

Received: 24 August 2022

Accepted: 5 September 2022

Published: 27 September 2022

Publisher's Note: MDPI stays neutral with regard to jurisdictional claims in published maps and institutional affiliations.



Copyright: © 2022 by the authors. Licensee MDPI, Basel, Switzerland. This article is an open access article distributed under the terms and conditions of the Creative Commons Attribution (CC BY) license (<https://creativecommons.org/licenses/by/4.0/>).

1. Introduction

At present, microwave absorbing materials (MAMs) are widely used in military and civil fields, such as stealth defense systems of aircraft, electromagnetic interference prevention, etc. [1–3]. Simple methods to manufacture high-performance MAMs have been a hot subject for decades. Studies have shown that a material's microwave absorbing performance (MAP) can be boosted by combining materials with dissipation and magnetic loss properties [4,5]. Researchers have identified a variety of microwave absorbing materials with good single loss mechanisms, such as single metals, alloys, carbon materials, conductive polymers with good properties, etc. However, these materials have a few drawbacks, including high density, complicated production processes, poor thermostability, and ease of oxidizing in air, and these drawbacks limit their applications. [6]. Among a variety of magnetic MAMs, Co has a more excellent absorption capability due to its large anisotropic field, high saturating strength of magnetization strength, and high-frequency Snoek's limit, but the absorption bandwidth is narrow due to eddy current loss, impedance mismatch, and lack of dielectric loss. Additionally, in the past few years, manganese oxides have been widely studied in several fields due to their low cost and abundant resources [7], such as Fe/MnO@C composites [8] and Co/MnO composites [9], which show excellent electromagnetic MAPs due to the extended electromagnetic microwave path and polarization loss.

In order to obtain outstanding MAPs, two or more composite materials can be used together to regulate electromagnetic parameters and impedance matching. For example, carbon-containing materials (carbon fibers, porous carbon nanospheres, carbon-based nanotubes etc.) [10–12] have been used in combination with other metal cations. For example, Zhou et al. prepared metal-organic framework (MOF)-derived porous metal/C composites (rod-like Co/ZnO/C composites) [13]. Such methods can achieve better electromagnetic MAPs. Multi-component absorbers consistently exhibit a wider range of microwave absorption spectra and stronger reflection loss (RL) than single-type absorbers [14]. In addition to the inter-matching between magnetic and dielectric elements, microstructure greatly influences the MAPs of composites. The core-shell structure of MAMs has recently received much attention. Such unique multilayer microstructures not only provide a significant benefit to microwave absorption due to their multilayer polarization, multiple reflections with microporous interfaces, and cooperative behavior, but also produce a high degree of chemical homogeneity by preventing the agglomeration of metal particles, making composite materials much more effective than single-component absorbers [15,16]. Liu et al. [17] successfully prepared core-shell $\text{Fe}_3\text{O}_4@\text{C}$. They found that a metal oxide surface coated with a carbon layer could improve the complex dielectric constant and the characteristic impedance matching, which significantly enhancing microwave absorption. Therefore, we infer that the yolk-shell microspheres combining dielectric carbon shells and magnetic MnO-Co cores can produce multiple reflective losses. This is due to the effective gap between magnetic and dielectric elements, and the impedance match allows the complex permittivity and permeability of the materials to be elevated.

Herein, we introduce a facile one-pot method to produce yolk core-shell structure MnO-Co@C nanospheres via in-situ reduction. The thickness of the carbon shell could be managed by regulating the volume of resorcinol and formaldehyde. The research revealed that the carbon shell can inhibit the agglomeration of MnO-Co nanospheres and adjust the complex dielectric constant of the material so that MnO-Co@C nanospheres have a stronger magnetic loss capability. The resistance matching of the material is improved, and the MAPs of the material are enhanced. These results may provide new ideas for improving conventional MAMs.

2. Experimental Section

2.1. Chemicals

All chemicals are for straight use (analytical grade drugs). Manganese acetate tetrahydrate ($\text{Mn}(\text{CH}_3\text{COO})_2 \cdot 4\text{H}_2\text{O}$), cobalt acetate tetrahydrate ($\text{Co}(\text{CH}_3\text{COO})_2 \cdot 4\text{H}_2\text{O}$), polyvinylpyrrolidone (PVP), ethylene glycol ($(\text{CH}_2\text{OH})_2$), resorcinol, ethanol ($\text{C}_2\text{H}_6\text{OH}$), formaldehyde (37%) and ammonia ($\text{NH}_3 \cdot \text{H}_2\text{O}$, 26%) were purchased from Sinopharm Chemical Reagent, Co., Ltd. (Shenyang, Liaoning, China). The water used throughout the experiment was deionized water.

2.2. The Preparation of MnCo_2O_4 Nanospheres

The preparation process of MnCo_2O_4 nanospheres is described in [18]. Briefly, 3.0 g of PVP was dissolved in 250 mL of $(\text{CH}_2\text{OH})_2$ and agitated for one hour. Next, 2.5 mmol of $\text{Mn}(\text{CH}_3\text{COO})_2 \cdot 4\text{H}_2\text{O}$ and 5.0 mmol of $\text{Co}(\text{CH}_3\text{COO})_2 \cdot 4\text{H}_2\text{O}$ were dissolved in the solution and stirred for one hour. The mixed solution was then transferred to a 500 mL round bottom flask, heated at 160 °C for 5 h, and naturally chilled to room temperature. Then, the reaction was centrifuged (8000 rpm), cleaned with ethanol, and dried in an oven at 80 °C for 12 h. The reaction was heated to 400 °C at 0.5 °C/min and held for 2 h to obtain MnCo_2O_4 nanospheres.

2.3. The Preparation of Core-Shell MnO-Co@C Nanospheres

Core-shell MnO-Co@C nanospheres were generated by a classical in situ polymerization and high-temperature carbonization method [19,20]. In short, 0.3 g of synthesized MnCo_2O_4 material was dispersed in a mixing solution that included 32 mL $\text{C}_2\text{H}_6\text{OH}$, 80 mL

deionized water, and 0.4 mL $\text{NH}_3 \cdot \text{H}_2\text{O}$. This solution was sonicated for 30 min and then magnetic stirred for 15 min. Resorcinol was added, the solution was stirred for 30 min, and then the formaldehyde was added. Next, the solution was agitated at room condition for 12 h, washed with deionized water and ethanol, and dried to obtain MnCo_2O_4 @phenolic resin, which was transferred to a tube furnace and held for 3 h under argon protective gas using $1^\circ\text{C}/\text{min}$ ramp to 750°C . Three samples were produced in this way, using different amounts of resorcinol and formaldehyde. The samples were labeled MnO-Co@C-0.2 , MnO-Co@C-0.3 , and MnO-Co@C-0.4 , and the addition amounts of resorcinol and formaldehyde for the three samples were 0.2 and 0.28, 0.3 and 0.42, and 0.4 and 0.56, respectively.

2.4. Characterization

A characterization of the constituent phases and the crystal structure of the samples was carried out by X-ray powder diffraction (XRD; smartlab9, Rigaku, Tokyo, Japan, Cu-K α source (40 kV, 200 mA)). The surface appearance and dimensional information of the material were assessed by scanning electron microscopy (SEM; JSM-7001F, JEOL, Tokyo, Japan). The element distribution inside the material and the internal morphology was observed by transmission electron microscopy (TEM; JEM-2100F, JEOL, Tokyo, Japan). X-ray photoelectron spectroscopy (XPS) was used to analyze the chemical bonding states of the elements on the material surfaces, using an Axis Supra with an Al K α X-ray source. A vector network analysis (VNA; ENA-E5080B, Keysight, Colorado Springs, CO, USA) was used to measure the related factors of the absorbing material in the frequency series 2–18 GHz and used to calculate the reflection loss magnitude. The product was homogeneously mixed with paraffin wax in a mass ratio of 3:7 and pressed into a ring sample with an outside diameter of 7 mm, an inside diameter of 3 mm, and a depth of roughly 3 mm.

3. Results and Discussion

The composition procedure of the core-shell MnO-Co@C nanospheres is shown in Figure 1. Mesoporous MnCo_2O_4 nanospheres with a mean diameter of approximately 500 nm were synthesized by a polyvinylpyrrolidone (PVP)-assisted solvothermal method. Then resorcinol and formaldehyde were used to form a layer of phenolic resin developed on the interface of MnCo_2O_4 . Finally, the precursor material is carbonized and reverted in a high-temperature shielding atmosphere to obtain multinuclear yolk-shell MnO-Co@C structures.

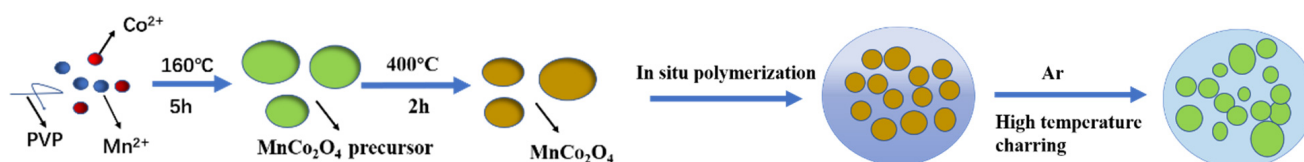


Figure 1. Schematic illustration of the composite process for core-shell MnO-Co@C nanospheres.

Figure 2 shows the morphology of MnCo_2O_4 nanospheres and MnO-Co@C nanospheres. Figure 3a shows that the average size of the diameter of the prepared MnCo_2O_4 nanospheres is about 500 nm, and the shrinkage shape of the nanoparticles becomes irregularly wrapped inside the carbon layer after in situ polymerization and calcination at 750°C . Combined with the XRD figure, it can be known that the internal nanoparticles were reduced to MnO-Co , and a small agglomeration of MnO-Co@C nanospheres occurred with the increase of the carbon amount. The TEM shows that the small metal nanoparticles are amorphyously distributed inside the carbon layer, and the carbon layer is uneven and microporous, thus increasing the multiple reflections of the material and providing reflection channels.

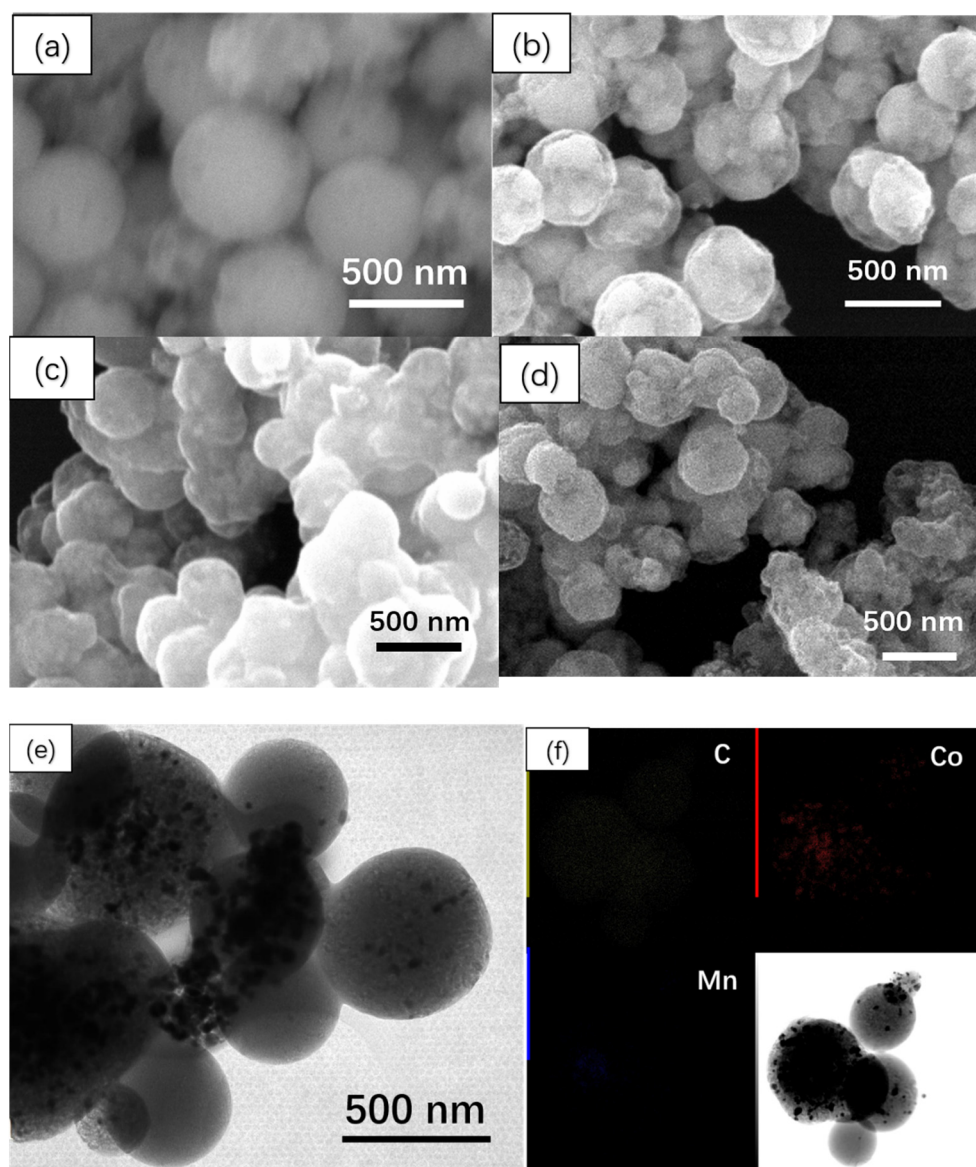


Figure 2. SEM images of MnCo_2O_4 (a), MnO-Co@C-0.2 (b), MnO-Co@C-0.3 (c), and MnO-Co@C-0.4 (d). TEM images of MnO-Co@C-0.3 (e), and elemental mapping distribution of MnO-Co@C-0.3 (f).

Figure 3a shows the XRD results of MnO-Co@C-0.2 , MnO-Co@C-0.3 and MnO-Co@C-0.4 . The diffraction peaks at 44.2° , 51.5° , and 75.8° for all the samples matches the (111), (200) and (220) planes of fcc Co (JCPDS 15-0806). The diffraction peaks at 35° , 40.7° , 58.9° , 70.4° , and 74° all match the (111), (200), (220), (311), (222) planes of MnO (JCPDS 75-0626). It was demonstrated that carbonizing at 750°C is sufficient to help the carbon to fully reduce the cobalt metal, while the MnO was not reduced [7,21]. It can be seen from the intensity of the peaks that the content of Co is higher than that of MnO. As we can see, with the increase of carbon content, the intensity of peaks of Co and MnO do not show significant differences. In the sense, we assume that the metallic Co can be easily reduced leaving the MnO dispersed around the Co and carbon shell, giving rise to the formation of multiple interfaces within this unique core-shell structure. Consequently, the presence of metallic Co and MnO increases the interfacial species of the core-shell structure. No significant characteristic peaks of impurities were found in all XRD plots, indicating the high purity of the prepared samples.

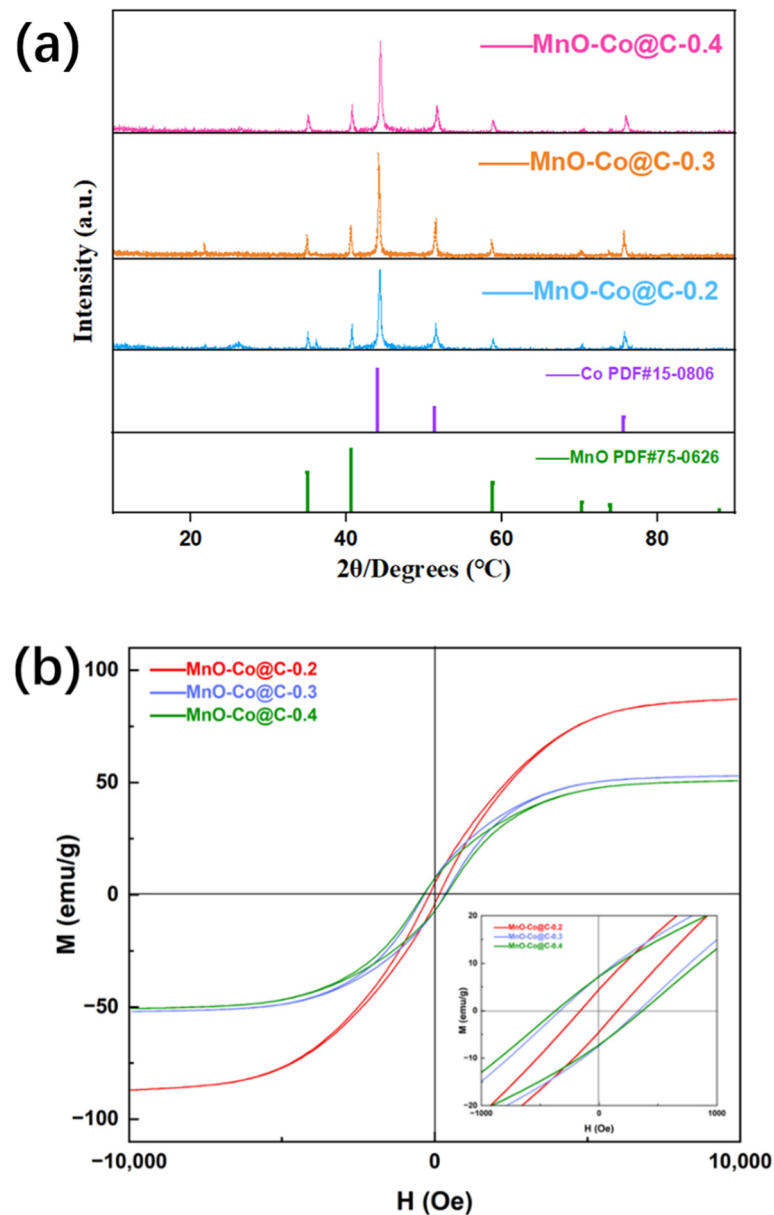


Figure 3. (a) The XRD pattern of MnO-Co@C-0.2, MnO-Co@C-0.3, and MnO-Co@C-0.4, (b) hysteresis loops of MnO-Co@C-0.2, MnO-Co@C-0.3, and MnO-Co@C-0.4.

The hysteresis lines of MnO-Co@C-0.2, MnO-Co@C-0.3, and MnO-Co@C-0.4 are shown in Figure 3b. According to these M-H curves, we can see that the saturation magnetization strength of the samples are 87.113 emu/g, 52.487 emu/g, and 50.746 emu/g, respectively. As you may observe from the graph, the material’s saturation magnetization strength decreases steadily with the addition of carbon content. For ferromagnetic MAMs, the initial magnetic permeability (μ_i) can be expressed as [22]:

$$\mu_i = \frac{M_s^2}{akH_cM_s + b\lambda\bar{\zeta}} \quad (1)$$

where a and b are two constants determined by the material composition, M_s is the saturation magnetization strength, H_c is the coercivity, λ is the magnetostriction constant, and $\bar{\zeta}$ is the elastic strain parameter of the crystal. An increase in the magnetic powder μ_i usually implies an increase in the magnetic loss potential, and the high M_s and low H_c also favor an increase in the magnetic loss potential.

The surface chemical composition and valence states of MnO-Co@C ternary nanocomposites were detected by X-ray photoelectron spectroscopy (XPS), and we can observe from Figure 4 that MnO-Co@C-0.3 has four characteristic peaks belonging to C 1s, O 1s, Co 2p, and Mn 2p, respectively. The characteristic peaks can be seen in the high-resolution spectra of C 1s at 283.8eV, 285eV, and 288.4eV, respectively, attributable to C=C, C-O, and O=C-C [23,24]. Co 2p can be adapted to 6 different feature peaks. The characteristic peaks at 779.2 eV and 794.6 eV belong to metallic Co, the feature peaks at 780.6 and 796.3 eV match the Co-O bond, and the remaining feature peaks at 786.8 eV and 803 eV can correspond to the satellite peaks [24]. Mn 2p can be fitted as 2 distinct feature peaks at 652.5 eV and 640.5 eV belonging to Mn²⁺ [25].

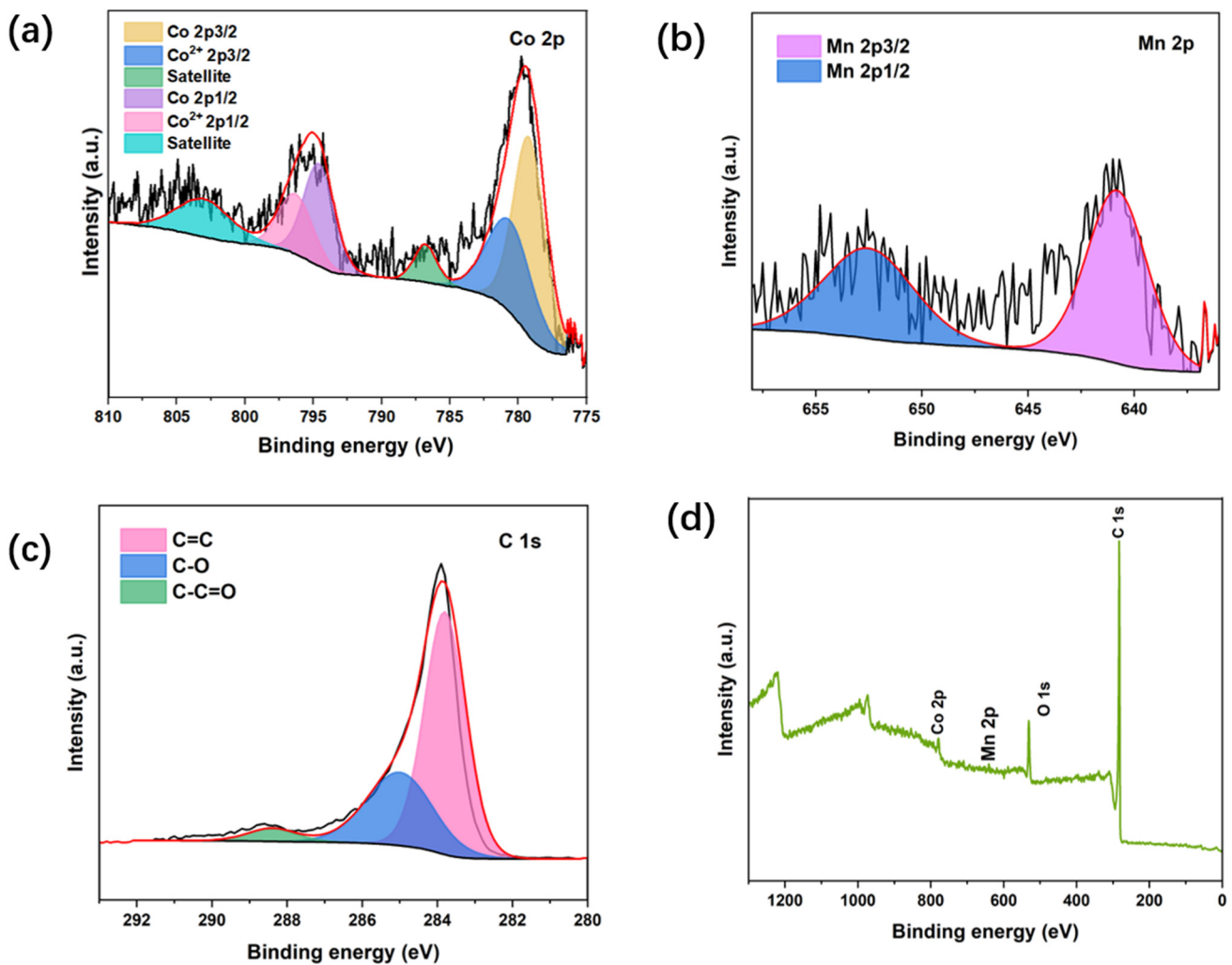


Figure 4. (a–c) high-resolution spectra Co 2p, Mn 2p, and C 1s, (d) Full scan XPS spectra of MnO-Co@C-0.3.

The reflection loss (RL) associated with the complex permittivity ($\epsilon_r = \epsilon' - j\epsilon''$) and permeability ($\mu_r = \mu' - j\mu''$) was measured in the range of 2–18 GHz to evaluate the MAPs of the composite, based on the transmission line theory [26]:

$$Z_{in} = Z_0 \sqrt{\mu_r/\epsilon_r} \tan h \left| j \left(\frac{2\pi f d}{c} \right) \sqrt{\epsilon_r \mu_r} \right| \quad (2)$$

$$RL(dB) = 20 \log \left| \frac{Z_{in} - Z_0}{Z_{in} + Z_0} \right| \quad (3)$$

where Z_{in} is the input resistance of the absorbers, Z_0 is the free space resistance, c is the velocity of light, and d is the thickening of the absorbers. The real part (ϵ' , μ') indicates the storage capacity of microwave energy, and the imaginary part (ϵ'' , μ'') indicates the ability to dissipate electromagnetic microwaves.

Figure 5a displays ϵ' values of MnO-Co@C-0.2, MnO-Co@C-0.3, and MnO-Co@C-0.4 in the frequency range of 2–18 GHz. We can observe that the value of MnO-Co@C-0.3 and MnO-Co@C-0.4 are relatively close and fall slightly in the range of 2–16 GHz. The ϵ' value of MnO-Co@C-0.2 is approximately 5.5 and remains almost unchanged. On the ground of free electron theory, it is proposed that the imaginary part of the complex permittivity can be redefined as $\epsilon'' \approx 1/2\pi\rho f\epsilon_0$ [27], where ρ is the resistivity and ϵ_0 is the free space permittivity. It is known that the value of ϵ'' is influenced by the conductivity, and the larger the conductivity, the larger the value of ϵ'' . The gradual increase in the ϵ'' values of the samples may be owing to the high cobalt metal content, and the graphitization of the material with the addition of resorcinol and formaldehyde. The dielectric tangent loss factor ($\tan \delta_\epsilon = \epsilon''/\epsilon'$) [28] is used to express the dielectric loss capability of the material. We can find that the value of $\tan \delta_\epsilon$ for MnO-Co@C-0.3 and MnO-Co@C-0.4 increases relative to the value of MnO-Co@C-0.2, fluctuating around 0.4, indicating that the dielectric loss capability of MnO-Co@C-0.3 and MnO-Co@C-0.4 is more significant than that of MnO-Co@C-0.2. We can observe from Figure 5c,d that the values of μ' and μ'' of all the three samples do not vary much, and the values are close to each other, with the value of μ' fluctuating around 1 and μ'' around 0. Similarly, the $\tan \delta_\mu = \mu''/\mu'$ [28] does not show much difference. It is possible to assume that the magnetic properties of the samples are not strong. The magnetic loss comes from the hysteresis, category wall resonance, ferromagnetic resonance, and eddy currents effects [29]. Hysteresis losses are insignificant in weaker electric fields, and domain wall resonance losses usually occur in lower frequencies (MHz) [30]. Therefore, the natural ferromagnetic resonance and eddy currents effects are commonly considered the major loss mechanisms of ferromagnetic absorbers at higher frequencies (GHz). The eddy current losses can be stated as [31]:

$$\mu'' = 2\pi\mu_0(\mu')^2\sigma d^2f/3 \quad (4)$$

where σ is the electrical conductivity and μ_0 is the magnetic conductivity in the presence of vacuum. The reflection loss is caused by the eddy current effect. $C_0 = \mu''(\mu')^{-2}f^{-1}$ When the frequency changes, C_0 is a constant, indicating the existence of eddy current loss in the material [32].

The ability of a material to dissipate electromagnetic energy can be quantified by the attenuation coefficient α , expressed by the formula [21]:

$$\alpha = \left(\frac{\sqrt{2\pi}f}{c} \right) \sqrt{\mu_r''\epsilon_r'' - \mu_r'\epsilon_r'} + \sqrt{(\mu_r''\epsilon_r'' - \mu_r'\epsilon_r')^2 + (\mu_r''\epsilon_r' - \mu_r'\epsilon_r'')^2} \quad (5)$$

From Figure 5h, it can be obtained that the α values of MnO-Co@C-0.2, MnO-Co@C-0.3, and MnO-Co@C-0.4 increase with the growth of frequency, and the values of MnO-Co@C-0.3 and MnO-Co@C-0.4 are higher than MnO-Co@C-0.2. It indicates that the electromagnetic dissipation capability of MnO-Co@C-0.3 and MnO-Co@C-0.4 is higher in the region of 2–18 GHz.

According to Equations (2) and (3), the correlation between the thickness of the relevant EMW absorbing material and the reflection loss (RL) in the spectrum of frequencies from 2–18 GHz can be calculated. Figure 6 illustrates the reflection loss of MnO-Co@C-0.2, MnO-Co@C-0.3, and MnO-Co@C-0.4 corresponding to the frequency and thickness in the spectrum of frequencies region of 2–18 GHz. We can obtain from the Figure 6a that the MnO-Co@C-0.2 absorption effect is inferior. When the absorber's thickness is 1–5 mm, and the microwave frequency is 2–18 GHz, no RL value reaches the effective value of –10 dB (absorption of 90% of electromagnetic microwaves). As the amount of resorcinol

and formaldehyde increases, the carbon layer becomes thicker and has a good reduction effect on the alloy. The MAPs of MnO-Co@C-0.3 and MnO-Co@C-0.4 are much better than MnO-Co@C-0.2. For MnO-Co@C-0.3, when the absorber thickness is about 3 mm, the EAB_{max} value reaches 3.3 GHz and the RL_{min} is -23.8 dB. The addition of resorcinol and formaldehyde further increases the absorbing effect of the materials. Thus, we reasoned that MnO-Co@C-0.3 has the best ratio. We can infer that as the carbon content increases, the amount of Co being reduced gradually increases, the non-homogeneous MnO-Co@C interface gradually increases, and the interfacial polarization is enhanced. As the carbon layer has a large number of dipoles, polarization loss is generated, which increases the dielectric loss of the material. The exchange resonance leads to an increase in magnetic loss, which promotes a good impedance match and increases the overall MAPs of the material. However, further increases of carbon content will not help much, as MnO-Co@C-0.4 did not perform better. The above results show that the spherical yolk core-shell MnO-Co@C material with a reasonable carbon content ratio can achieve broadband EMW absorption with good overall performance. This excellent microwave absorption performance originates from the impedance matching of the composite; the cooperation between dielectric losses and magnetic losses.

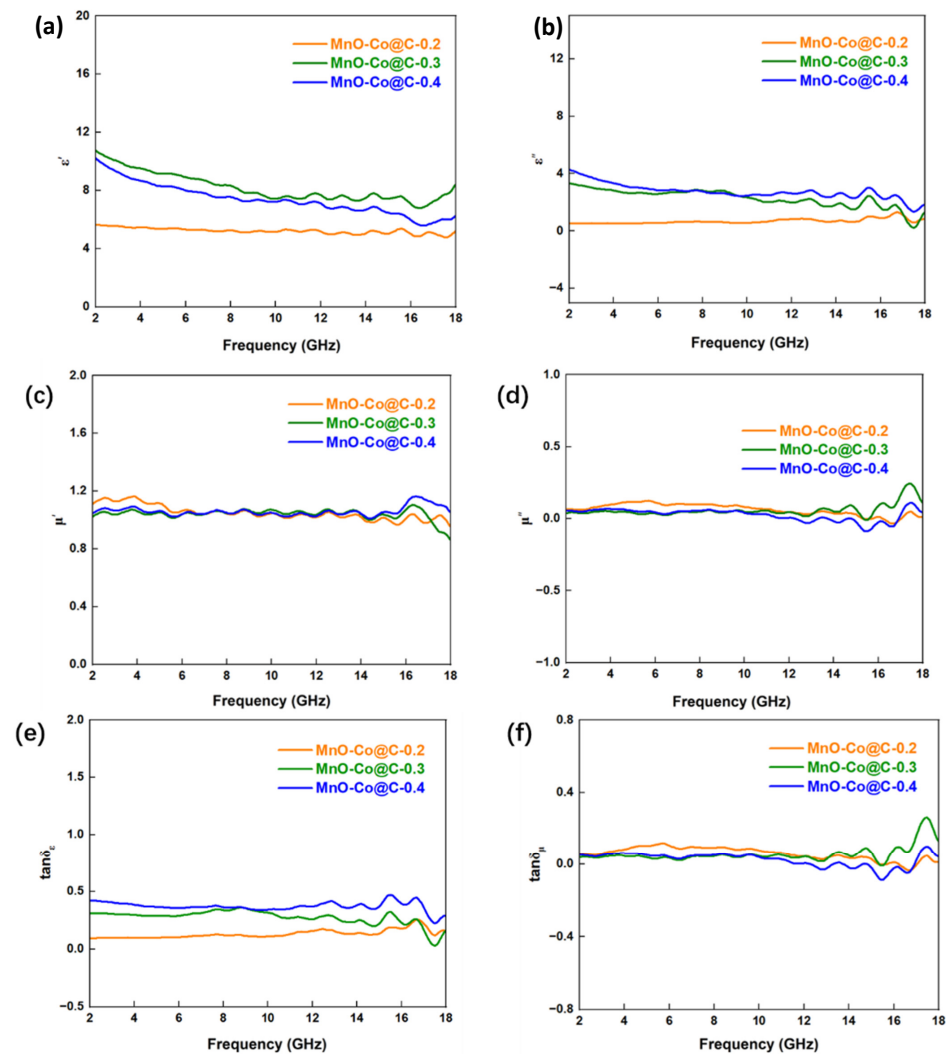


Figure 5. Cont.

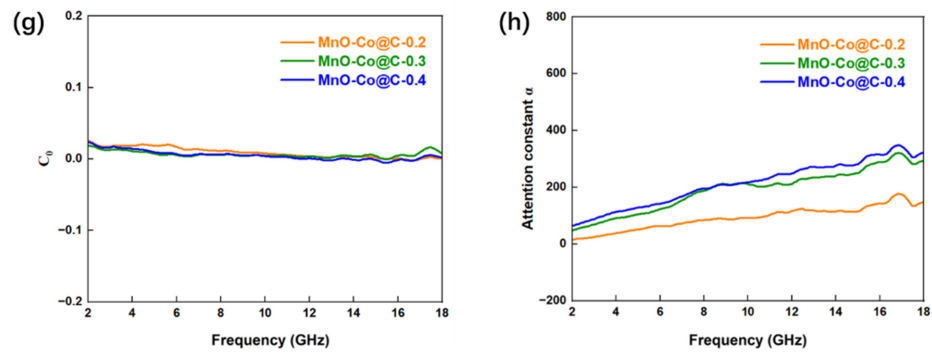


Figure 5. Electromagnetic parameters of MnO-Co@C-0.2, MnO-Co@C-0.3, and MnO-Co@C-0.4: (a) ϵ' , (b) ϵ'' , (c) μ' (d) μ'' , (e) the dielectric loss tangent factor $\tan\delta_\epsilon$, (f) the magnetic loss tangent factor $\tan\delta_{\mu}$, (g) C_0 , (h) attention constant α .

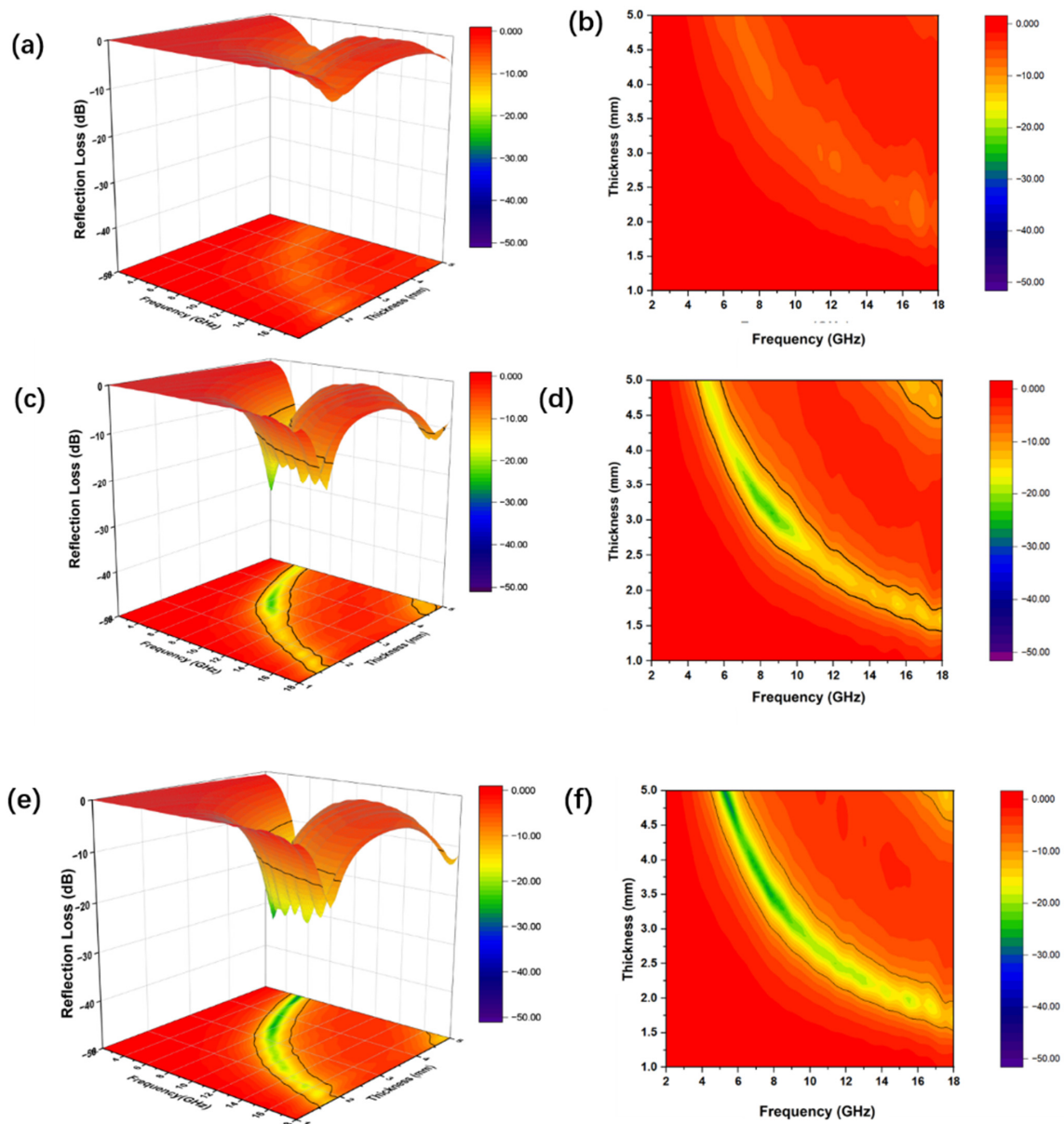


Figure 6. Reflection loss values in the frequency of 2–18 GHz for (a,b) MnO-Co@C-0.2; (c,d) MnO-Co@C-0.3; (e,f) MnO-Co@C-0.4.

4. Conclusions

In conclusion, a novel metal-metal oxide-carbon material interface was designed to form a special yolk core-shell structure. The spherical yolk core-shell MnO-Co@C material exhibits good EMW absorption performance and achieves the best reflection loss value of -23.8 dB and the EAB_{max} reaches 3.3 GHz when the surface thickness is 3 mm. Both of the dielectric and magnetic losses, and the unique yolk core-shell structure, all contribute significantly to the material's excellent microwave absorption. Core-shell MnO-Co@C nanospheres have the advantages of a simple preparation method, enhanced wave absorption performance, wide absorption bandwidth, and low density, making them a great application prospect in microwave absorption.

Author Contributions: Conceptualization, M.Z. and X.S.; methodology, S.S.; software, Z.X.; validation, J.W., S.S. and M.Z.; formal analysis, M.Z.; investigation, Z.X.; resources, S.S.; data curation, X.S.; writing—original draft preparation, Z.X.; writing—review and editing, M.Z.; visualization, M.Z.; supervision, M.Z.; project administration, J.W.; funding acquisition, M.Z. All authors have read and agreed to the published version of the manuscript.

Funding: This research was funded by National Natural Science Foundation of China (52072063), Research start-up fund of Foshan Graduate School of Northeastern University.

Institutional Review Board Statement: Not applicable.

Informed Consent Statement: Not applicable.

Data Availability Statement: Not applicable.

Conflicts of Interest: The authors declare no conflict of interest.

References

1. Micheli, D.; Vricella, A.; Pastore, R.; Marchetti, M. Synthesis and electromagnetic characterization of frequency selective radar absorbing materials using carbon nanopowders. *Carbon* **2014**, *77*, 756–774. [[CrossRef](#)]
2. Shahzad, F.; Alhabeab, M.; Hatter, C.B.; Anasori, B.; Hong, S.M.; Koo, C.M.; Gogotsi, Y. Electromagnetic interference shielding with 2D transition metal carbides (MXenes). *Science* **2016**, *353*, 1137–1140. [[CrossRef](#)]
3. Giannakopoulou, T.; Kompotiatis, L.; Kontogeorgakos, A.; Kordas, G. Microwave behavior of ferrites prepared via sol-gel method. *J. Magn. Magn. Mater.* **2002**, *246*, 360–365. [[CrossRef](#)]
4. Wang, J.; Liu, L.; Jiao, S.; Ma, K.; Lv, J.; Yang, J. Hierarchical Carbon Fiber@MXene@MoS₂ Core-sheath Synergistic Microstructure for Tunable and Efficient Microwave Absorption. *Adv. Funct. Mater.* **2020**, *30*, 2002595. [[CrossRef](#)]
5. Zhang, D.; Liu, T.; Cheng, J.; Cao, Q.; Zheng, G.; Liang, S.; Wang, H.; Cao, M.S. Lightweight and High-Performance Microwave Absorber Based on 2D WS₂-RGO Heterostructures. *Nano-Micro Lett.* **2019**, *11*, 38. [[CrossRef](#)]
6. Ma, R.-T.; Shang, H.-Y.; Wang, X.; Jiang, D. Dielectric, magnetic and microwave absorbing properties of polyaniline-Co_{0.7}Cr_{0.1}Zn_{0.2}Fe₂O₄ composites. *Rare Met.* **2017**, *36*, 118–122. [[CrossRef](#)]
7. Qiu, Y.; Wen, B.; Yang, H.; Lin, Y.; Cheng, Y.; Jin, L. MOFs derived Co@C/MnO nanorods with enhanced interfacial polarization for boosting the electromagnetic wave absorption. *J. Colloid Interface Sci.* **2021**, *602*, 242–250. [[CrossRef](#)]
8. He, G.; Duan, Y.; Pang, H. Microwave Absorption of Crystalline Fe/MnO@C Nanocapsules Embedded in Amorphous Carbon. *Nano-Micro Lett.* **2020**, *12*, 57. [[CrossRef](#)]
9. Xu, D.; Qiao, J.; Wu, N.; Liu, W.; Wang, F.; Lv, L.; Pan, J.; Dong, Y.; Liu, J. Facile Synthesis of Three-Dimensional Porous Co/MnO Composites Derived from Bimetal Oxides for Highly Efficient Electromagnetic Wave Absorption. *ACS Sustain. Chem. Eng.* **2019**, *7*, 8687–8695. [[CrossRef](#)]
10. Shu, R.; Li, W.; Zhou, X.; Tian, D.; Zhang, G.; Gan, Y.; Shi, J.; He, J. Facile preparation and microwave absorption properties of RGO/MWCNTs/ZnFe₂O₄ hybrid nanocomposites. *J. Alloys Compd.* **2018**, *743*, 163–174. [[CrossRef](#)]
11. Liu, P.-B.; Huang, Y.; Sun, X. Excellent Electromagnetic Absorption Properties of Poly(3,4-ethylenedioxythiophene)-Reduced Graphene Oxide-Co₃O₄ Composites Prepared by a Hydrothermal Method. *ACS Appl. Mater. Interfaces* **2013**, *5*, 12355–12360. [[CrossRef](#)] [[PubMed](#)]
12. Li, X.; Feng, J.; Du, Y.; Bai, J.; Fan, H.; Zhang, H.; Peng, Y.; Li, F. One-pot synthesis of CoFe₂O₄/graphene oxide hybrids and their conversion into FeCo/graphene hybrids for lightweight and highly efficient microwave absorber. *J. Mater. Chem. A* **2015**, *3*, 5535–5546. [[CrossRef](#)]
13. Liao, Q.; He, M.; Zhou, Y.; Nie, S.; Wang, Y.; Hu, S.; Yang, H.; Li, H.; Tong, Y. Highly Cuboid-Shaped Heterobimetallic Metal-Organic Frameworks Derived from Porous Co/ZnO/C Microrods with Improved Electromagnetic Wave Absorption Capabilities. *ACS Appl. Mater. Interfaces* **2018**, *10*, 29136–29144. [[CrossRef](#)]

14. Yu, M.; Liang, C.; Liu, M.; Liu, X.; Yuan, K.; Cao, H.; Che, R. Yolk-shell Fe₃O₄@ZrO₂ prepared by a tunable polymer surfactant assisted sol-gel method for high temperature stable microwave absorption. *J. Mater. Chem. C* **2014**, *2*, 7275–7283. [[CrossRef](#)]
15. Tian, C.; Du, Y.; Xu, P.; Qiang, R.; Wang, Y.; Ding, D.; Xue, J.; Ma, J.; Zhao, H.; Han, X. Constructing Uniform Core-Shell PPy@PANI Composites with Tunable Shell Thickness toward Enhancement in Microwave Absorption. *ACS Appl. Mater. Interfaces* **2015**, *7*, 20090–20099. [[CrossRef](#)]
16. Liu, X.G.; Li, B.; Geng, D.Y.; Cui, W.B.; Yang, F.; Xie, Z.G.; Kang, D.J.; Zhang, Z.D. (Fe, Ni)/C nanocapsules for electromagnetic-wave-absorber in the whole Ku-band. *Carbon* **2009**, *47*, 470–474. [[CrossRef](#)]
17. Liu, X.; Cui, X.; Chen, Y.; Zhang, X.-J.; Yu, R.; Wang, G.-S.; Ma, H. Modulation of electromagnetic wave absorption by carbon shell thickness in carbon encapsulated magnetite nanospindles-poly (vinylidene fluoride) composites. *Carbon* **2015**, *95*, 870–878. [[CrossRef](#)]
18. Zhou, S.; Luo, X.; Chen, L.; Xu, C.; Yan, D. MnCo₂O₄ nanospheres for improved lithium storage performance. *Ceram. Int.* **2018**, *44*, 17858–17863. [[CrossRef](#)]
19. Qiao, Z.-A.; Guo, B.; Binder, A.J.; Chen, J.; Veith, G.M.; Dai, S. Controlled Synthesis of Mesoporous Carbon Nanostructures via a “Silica-Assisted” Strategy. *Nano Lett.* **2013**, *13*, 207–212. [[CrossRef](#)]
20. Meng, X.; Liu, Y.; Han, G.; Yang, W.; Yu, Y. Three-dimensional (Fe₃O₄/ZnO)@C Double-core@shell porous nanocomposites with enhanced broadband microwave absorption. *Carbon* **2020**, *162*, 356–364. [[CrossRef](#)]
21. Ding, D.; Wang, Y.; Li, X.; Qiang, R.; Xu, P.; Chu, W.; Han, X.; Du, Y. Rational design of core-shell Co@C microspheres for high-performance microwave absorption. *Carbon* **2017**, *111*, 722–732. [[CrossRef](#)]
22. Saini, P.; Choudhary, V.; Vijayan, N.; Kotnala, R.K. Improved Electromagnetic Interference Shielding Response of Poly(aniline)-Coated Fabrics Containing Dielectric and Magnetic Nanoparticles. *J. Phys. Chem. C* **2012**, *116*, 13403–13412. [[CrossRef](#)]
23. Wu, Y.; Shu, R.; Zhang, J.; Wan, Z.; Shi, J.; Liu, Y.; Zhao, G.; Zheng, M. Oxygen vacancies regulated microwave absorption properties of reduced graphene oxide/multi-walled carbon nanotubes/cerium oxide ternary nanocomposite. *J. Alloys Compd.* **2020**, *819*, 152944. [[CrossRef](#)]
24. Wang, J.; Jia, Z.; Liu, X.; Dou, J.; Xu, B.; Wang, B.; Wu, G. Construction of 1D Heterostructure NiCo@C/ZnO Nanorod with Enhanced Microwave Absorption. *Nano-Micro Lett.* **2021**, *13*, 175. [[CrossRef](#)] [[PubMed](#)]
25. Samanta, A.; Barman, B.K.; Mallick, S.; Raj, C.R. Three-Dimensional Nitrogen-Doped Graphitic Carbon-Encapsulated MnO-Co Heterostructure: A Bifunctional Energy Storage Material for Zn-Ion and Zn-Air Batteries. *ACS Appl. Energy Mater.* **2020**, *3*, 10108–10118. [[CrossRef](#)]
26. Kuchi, R.; Sharma, M.; Lee, S.W.; Kim, D.; Jung, N.; Jeong, J.-R. Rational design of carbon shell-encapsulated cobalt nanospheres to enhance microwave absorption performance. *Prog. Nat. Sci. Mater. Int.* **2019**, *29*, 88–93. [[CrossRef](#)]
27. Ren, F.; Yu, H.; Wang, L.; Saleem, M.; Tian, Z.; Ren, P. Current progress on the modification of carbon nanotubes and their application in electromagnetic wave absorption. *RSC Adv.* **2014**, *4*, 14419–14431. [[CrossRef](#)]
28. Panwar, R.; Puthucheri, S.; Singh, D.; Agarwala, V.; Lee, J.-R. Microwave absorption properties of FSS-impacted composites as a broadband microwave absorber. *Adv. Compos. Mater.* **2017**, *26*, 99–113. [[CrossRef](#)]
29. Wen, B.; Cao, M.-S.; Hou, Z.-L.; Song, W.-L.; Zhang, L.; Lu, M.-M.; Jin, H.-B.; Fang, X.-Y.; Wang, W.-Z.; Yuan, J. Temperature dependent microwave attenuation behavior for carbon-nanotube/silica composites. *Carbon* **2013**, *65*, 124–139. [[CrossRef](#)]
30. Wu, M.; Zhang, Y.D.; Hui, S.; Xiao, T.D.; Ge, S.; Hines, W.A.; Budnick, J.I.; Taylor, G.W. Microwave magnetic properties of Co₅₀/(SiO₂)₅₀ nanoparticles. *Appl. Phys. Lett.* **2002**, *80*, 4404–4406. [[CrossRef](#)]
31. Zhu, J.; Wei, S.; Haldolaarachchige, N.; Young, D.P.; Guo, Z. Electromagnetic Field Shielding Polyurethane Nanocomposites Reinforced with Core-Shell Fe-Silica Nanoparticles. *J. Phys. Chem. C* **2011**, *115*, 15304–15310. [[CrossRef](#)]
32. Jian, X.; Wu, B.; Wei, Y.; Dou, S.X.; Wang, X.; He, W.; Mahmood, N. Facile Synthesis of Fe₃O₄/GCs Composites and Their Enhanced Microwave Absorption Properties. *ACS Appl. Mater. Interfaces* **2016**, *8*, 6101–6109. [[CrossRef](#)] [[PubMed](#)]